



OPEN

# Experimental imaging properties of immersion microscale spherical lenses

SUBJECT AREAS:

MICRO-OPTICS  
IMAGING AND SENSINGRan Ye<sup>1</sup>, Yong-Hong Ye<sup>1</sup>, Hui Feng Ma<sup>2</sup>, Lingling Cao<sup>1</sup>, Jun Ma<sup>3</sup>, Frank Wyrowski<sup>4</sup>, Rui Shi<sup>4</sup>  
& Jia-Yu Zhang<sup>5</sup>Received  
23 October 2013Accepted  
27 December 2013Published  
20 January 2014Correspondence and  
requests for materials  
should be addressed to  
Y.-H.Y. (yeyonghong@  
njnu.edu.cn) or J.-Y.Z.  
(jyzhang@seu.edu.cn)

<sup>1</sup>Jiangsu Provincial Key Laboratory of Optoelectronic Technology, Department of Physics, Nanjing Normal University, Nanjing 210097, China, <sup>2</sup>State Key Laboratory of Millimeter Waves, Southeast University, Nanjing 210096, China, <sup>3</sup>School of Electronic and Optical Engineering, Nanjing University of Science and Technology, Nanjing 210094, China, <sup>4</sup>Institute of Applied Physics, Friedrich-Schiller-University Jena, Max-Wien-Platz 1, 07743 Jena, Germany, <sup>5</sup>Department of Electronic Engineering, Southeast University, Nanjing 210096, China.

Using the immersion lensing technique, the resolution of a conventional spherical lens can be improved by a factor of  $1/n$  over its value in air ( $n$ , the refractive index of the immersion medium). Depending on the relative position between an object and a lens, either a real or a virtual image is formed. Here we report a new physical phenomenon experimentally observed in the microscale lens imaging. We find that when a microscale spherical lens is semi-immersed in a medium, the resolution of the lens is improved as it can intercept more fine details of the object. However, the microscale lens has two image channels for the fine and coarse details and two images corresponding to the two components can be formed simultaneously. Our findings will advance the understanding of the super-resolution imaging mechanisms in microscale lenses.

In geometrical optics, it is well known that depending on the relative position between an object and a spherical lens, either a real or a virtual image is formed. Features of an object smaller than  $\lambda/2$  ( $\lambda$ , wavelength) cannot be imaged by the lens in the far-field due to Abbe's diffraction limit. Using the immersion lensing technique, the wavelength and hence the resolution can be improved by a factor of  $1/n$  over its value in air ( $n$ , the refractive index of the immersion medium)<sup>1,2</sup>. Microscale and nanoscale lenses can magnify and resolve features beyond the diffraction limit<sup>3–16</sup>. Still, either a real or a virtual image is observed in these lenses in the reported studies. Recently, the immersion lensing technique has also been applied to the microscale lenses<sup>14</sup>. Mason et al. have demonstrated that the focal spot size of a wavelength-scale solid immersion lens is greatly reduced<sup>15</sup>. Hao et al. have shown that the magnified virtual image has a sharper contrast when the microscale spherical lens is semi-immersed in liquid<sup>16</sup>. However, compared to the well-studied small lenses on the scale of  $\sim 1$  mm, the imaging properties of immersed microscale lenses are far less studied<sup>17–19</sup>. Here we report a new physical phenomenon experimentally observed in the microscale lens imaging when the lens is semi-immersed in a medium. If the object size is well beyond the diffraction limit, two images are formed simultaneously by a microscale spherical lens. One image is blurring, and it is formed by the small lateral wave vector (small- $k$ ) Fourier components of the object. This image formation can be explained by the combination of geometrical optics and near-field optics. The other image is sharper and clear, and it is formed by the large lateral wave vector (large- $k$ ) Fourier components of the object. Near-field magnification plays an important role in this image formation. Our experimental results reveal that when a microscale spherical lens is semi-immersed in a medium, it can intercept more large- $k$  Fourier components of the object, which means that the effective numerical aperture of the lens is increased. However, the microscale lens has two image channels. One channel transforms the small- $k$  Fourier components, while the other transforms the large- $k$  Fourier components. As the physical mechanism behind the microscale lens imaging remains to be further revealed<sup>20</sup>, our findings will advance the understanding of the super-resolution imaging mechanisms in microscale lenses.

## Results

Figure 1a illustrates the schematic of the experimental setup. Self-assembled polystyrene (PS) microsphere arrays were used as the image objects. In the experiments, two kinds of PS microspheres with different diameters (280 and 960 nm) were used. The samples were put under a Leica microscope, and the reflected images of the PS microsphere arrays through the 4.87- $\mu\text{m}$ -diameter silica microscale lens were observed and recorded by a 100 $\times$  (NA = 0.9) microscope objective with a CCD (charge-coupled device) camera. During the experiment, the

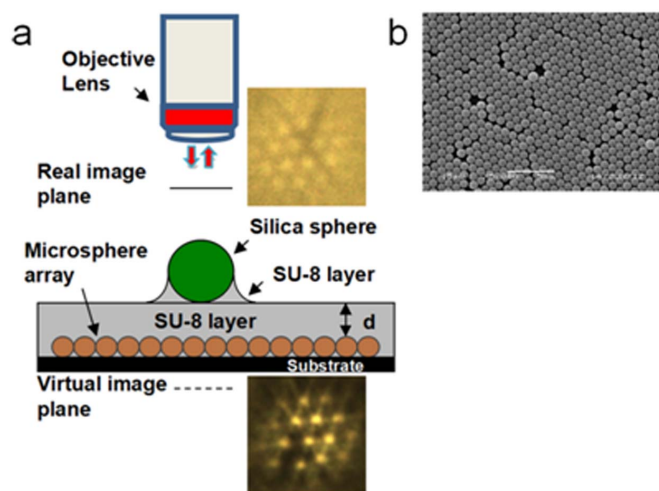


**Figure 1** | Schematic illustration of the experimental setup. (a) Schematic of the experimental setup. (b) SEM image of a self-assembled PS microsphere array. The diameter of the PS microspheres is 960 nm in this sample.

position of the microscope objective is moved in order to focus the formed images. In our experiments, if we observe that the depth of the image is below the focal plane of the silica microscale lens, the formed image is called a virtual image. Otherwise, the formed image is called a real image. When a SU-8 layer is coated on top of the objects, the Rayleigh resolution limit for point objects is  $229 \text{ nm}$  ( $r = 0.61\lambda/nNA$ ), here  $\lambda = 540 \text{ nm}$ ,  $n = 1.6$  (the refractive index of SU-8), and  $NA = 0.9^2$ . Therefore, the large objects (fabricated by the 960 nm microspheres) are well beyond the resolution limit, while the small objects (fabricated by the 280 nm microspheres) are close to the resolution limit. Fig. 1b shows the scanning electron microscope (SEM) image of a typical self-assembled PS microsphere array. The diameter of the PS microspheres is 960 nm in this sample. As shown in Fig. 1b, the microspheres are hexagonally close-packed with defects and multiple domains mainly due to the large size deviation of the microspheres (a standard deviation of 5–10%).

Fig. 2a–c shows the optical microscope images of a large object (fabricated with the 960 nm microspheres) at different distance between the object and the 4.87- $\mu\text{m}$ -diameter silica microscale lens (d). For these samples, the microscale lens are semi-immersed in the SU-8 resist, as shown in Fig. 2d. As shown in Fig. 2a, at  $d = 0$ , two virtual images are formed (image a-1 is clear, and image a-2 is blurring), and the magnification factor  $M$  is about  $2.08\times$  and  $3.07\times$  for the clear and blurring images, respectively. At  $d = 3.1$  and  $4.1 \mu\text{m}$ , a virtual image and a real image are observed, as shown in Fig. 2b, c. The virtual image is sharper and clear, the real image is blurring, and the two images are mutually inverted (as shown in the defects in Fig. 2b). The virtual image keeps the same orientation as the object. The optical image b-3 at the bottom of Fig. 2b is taken when the focal plane is on the 960 nm PS microspheres (the object). As shown in Fig. 2b, at  $d = 3.1 \mu\text{m}$ ,  $M$  of the virtual image is about  $1.52\times$  (b-1), while  $M$  of the real image is about  $-1.64\times$  (b-2). At  $d = 4.1 \mu\text{m}$ ,  $M$  is about  $1.51\times$  (c-1) and  $-1.19\times$  (c-2) for the virtual image and the real image, respectively. To clearly show the image process, a video that records the whole dynamic process (the focusing of the real image plane, then the object plane, and finally the virtual image plane) is also given (Supplementary Video 1). In this video,  $d$  is  $\sim 3.1 \mu\text{m}$ . We also replace the SU-8 resist with the index-matching oil, and let the lenses semi-immersed in the index-matching oil. The results are close to the ones shown in Fig. 2 (Supplementary Fig. S1). It should also be noted that the ordering of the PS microsphere array is not important in the image formation. The areas where the

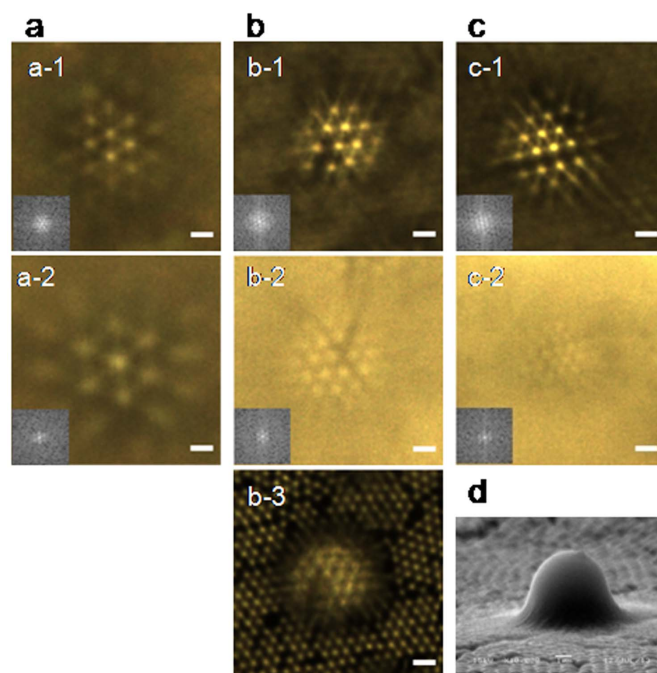


**Figure 2** | Optical images of a semi-immersed microscale lens on a large object at different distance  $d$ . (a)  $d = 0 \mu\text{m}$ , two virtual images are formed. (b)  $d = 3.1 \mu\text{m}$ , a virtual image (b-1) and a real image (b-2) are observed. Image b-3 is the image of the object. (c)  $d = 4.1 \mu\text{m}$ , a virtual image (c-1) and a real image (c-2) are observed. (d) SEM image of a semi-immersed microscale lens. The large object is fabricated with the 960 nm microspheres. The lens is semi-immersed in the SU-8 resist. The scale bar is  $2 \mu\text{m}$ .

microspheres are randomly packed are also observed, and we get similar results (Supplementary Fig. S2).

To explore the origin of the images observed in Fig. 2, the large object samples where the microscale lenses are not semi-immersed in the SU-8 resist are also studied. Fig. 3a–c is the optical images of the objects at different  $d$ , while Fig. 3d is the SEM image of a microscale lens which is not semi-immersed in the SU-8 resist. It is found that only one blurring image (either a real or a virtual image) is observed at the three distances studied here. As shown in Fig. 3a, at  $d = 0$ , a virtual image is formed and  $M$  is around  $4.05\times$ . When  $d$  is  $3.1$  or  $4.1 \mu\text{m}$ , a real image is formed, and  $M$  is about  $-1.14\times$  (Fig. 3b) or  $-0.85\times$  (Fig. 3c), respectively. Figure 3 indicates that the microscale lens should be semi-immersed in the SU-8 resist or the index-matching oil in order to observe the clear and sharper images in Fig. 2.

To further analyze the imaging behaviors of the microscale lens, the imaging properties of a microscale lens on a small object are also studied. Fig. 4a–c shows the optical microscope images of a small object (fabricated from the 280 nm PS microspheres) at different distance  $d$ . For these samples, the lenses are semi-immersed in the SU-8 resist. As shown in Fig. 4a–c, all the formed images are virtual images, and the images are clear and well-defined. The lens magnifies the underlying object, and  $M$  is about  $2.0\times$ ,  $1.51\times$ , and  $1.50\times$  when  $d$  is  $0$ ,  $3.1$ , and  $4.1 \mu\text{m}$ , respectively. A video that records the whole dynamic process is also given (Supplementary Video 2). In this video, only the focusing of the virtual image plane is observed.  $d$  is  $\sim 3.1 \mu\text{m}$ .

Our experimental results indicate that: (1) the formation of the blurred images only depends on the object size. In the large object samples (960 nm microspheres), we can always observe the blurred images in both semi-immersed and non-immersed cases. In the small object samples (280 nm microspheres), the blurred images cannot be observed in both semi-immersed and non-immersed

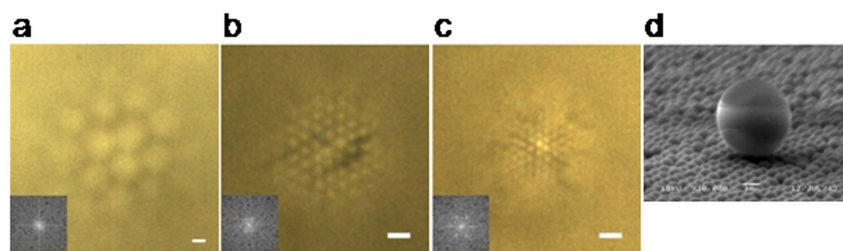


**Figure 3** | Optical images of a microscale lens on a large object at different distance  $d$ . (a)  $d = 0$ , a virtual image is formed. (b)  $d = 3.1 \mu\text{m}$ , a real image is formed. (c)  $d = 4.1 \mu\text{m}$ , a real image is formed. (d) SEM image of a microscale lens that is not semi-immersed in the SU-8 resist. The large object is fabricated with the 960 nm microspheres. The lens is not semi-immersed in the SU-8 resist. The scale bar is  $2 \mu\text{m}$ .

cases; (2) the clear images can only be observed when the microscale lens is semi-immersed in the SU-8 resist. This image formation does not depend on the object size. In both the large and small object samples, the clear images are observed as long as the lens is semi-immersed; (3) for the clear images, the magnification hardly changes when the distance  $d$  or the object size changes. The magnification  $M$  for the blurring images depends on the distance  $d$ .

The Fourier expansion in terms of the fields of a two-dimensional object is<sup>22</sup>

$$E(r,t) = \sum_{\sigma, k_x, k_y} E_{\sigma}(k_x, k_y) \exp(ik_z z + ik_x x + ik_y y - i\omega t) \quad (1)$$

here, the wavenumber components  $k_x$ ,  $k_y$ , and  $k_z$  associate with propagation in the  $x$ ,  $y$ , and  $z$  directions, and are related to the wavenumber  $k$  by  $k^2 = k_x^2 + k_y^2 + k_z^2$ . In free space, the propagation of light is  $k^2 = \left(\frac{\omega}{c}\right)^2$ , here,  $\omega$  is the angular frequency, and  $c$  is the speed of propagation. If the propagation axis is assumed to be along the  $z$  axis, the spatial Fourier components with lateral  $k$ -vectors  $k_x^2 + k_y^2 < \omega^2 c^{-2}$  are propagating waves ( $k_z = \sqrt{\omega^2 c^{-2} - k_x^2 - k_y^2}$ ), and the spatial components with lateral  $k$ -vectors ( $k_x^2 + k_y^2 > \omega^2 c^{-2}$ ) are evanescent waves ( $k_z = i\sqrt{k_x^2 + k_y^2 - \omega^2 c^{-2}}$ ). Objects contain information at many different spatial scales, from fine to coarse. Fine detail is equivalent to large- $k$  Fourier components, while coarse detail is equivalent to small- $k$  Fourier components.

The frequency spectra of the images in Figs. 2, 3, and 4 are calculated by Fourier analysis, and are also shown in the insets of the figures, with the low-frequencies located at the center and the high-frequencies at the corners. The frequency spectra show that the blurred images mainly have small- $k$  Fourier components, while the clear images have more large- $k$  components than the blurred images have. Therefore, we propose the blurring images in Figs. 2 and 3 are the small- $k$  Fourier components of the large objects, while

the clear and sharper images in Figs. 2 and 4 are the large- $k$  Fourier components of the objects. Here, both the small- $k$  and large- $k$  Fourier components are propagating waves as the two objects studied here are larger than the resolution limit.

The imaging properties of the microscale lens are first calculated by ZEMAX, a geometrical optics based ray-tracing program. When the lens is semi-immersed in the SU-8 resist, the focal plane of the object space from the center of the microsphere ( $F$ ) obtained from ZEMAX is  $5.9 \mu\text{m}$ . According to the paraxial ray-tracing formulae used in geometrical optics, the calculated magnification is  $1.70\times$  (virtual image),  $15.68\times$  (virtual image), and  $-9.49\times$  (real image) at  $d = 0, 3.1$ , and  $4.1 \mu\text{m}$ , respectively. When the lens is not semi-immersed in the SU-8 resist,  $F$  obtained from ZEMAX is  $4.6 \mu\text{m}$ , and the calculated  $M$  is  $2.11\times$ ,  $-5.08\times$ , and  $-2.42\times$  at  $d = 0, 3.1$ , and  $4.1 \mu\text{m}$ , respectively. Studies have show that the real  $F$  of a microscale lens is much shorter than the one expected from ray-tracing program due to near-field focusing (Supplementary Fig. S3)<sup>7</sup>.  $F$  is also calculated by CST (by calculating the exact solution of Maxwell's equation). When the lens is semi-immersed in the SU-8 resist, the  $F$  obtained from CST is  $3.5 \mu\text{m}$ . According to geometrical optics, the calculated magnification is  $3.31\times$ ,  $-1.71\times$ , and  $-1.15\times$  at  $d = 0, 3.1$ , and  $4.1 \mu\text{m}$ , respectively. When the lens is not semi-immersed in the SU-8 resist,  $F$  obtained from CST is  $3.0 \mu\text{m}$ , and the calculated magnification is  $5.40\times$ ,  $-1.18\times$ , and  $-0.85\times$  at  $d = 0, 3.1$ , and  $4.1 \mu\text{m}$ , respectively. The calculated magnifications using the shorter  $F$  from CST are very close to the experimental ones of the blurring images. Table 1 summarizes the magnifications of the images (both blurring and clear) obtained from both experiments and calculations. These results indicate that the blurring images formed from the small- $k$  Fourier components in Figs. 2 and 3 can be explained by geometrical optics by using the short  $F$  calculated from CST. As small objects have less small- $k$  Fourier components than large objects have, the blurred images formed by the small- $k$  components cannot be observed for the objects fabricated by the 280 nm microspheres.

To find out the origin of the clear images in Figs. 2 and 4, the electric field distribution of a microscale lens imaging system when the lens is semi-immersed or not semi-immersed in the SU-8 resist are simulated by CST. The object is set as a dipole. As shown in Fig. 5, when the lens is not semi-immersed in the SU-8 resist, only the small- $k$  Fourier components generated by an object are intercepted by the microscale lens, and a real image is formed. If the lens is semi-immersed in the SU-8 layer, more large- $k$  Fourier components will couple into the lens. The real image formed by the small- $k$  Fourier components still exists. Moreover, the large- $k$  components form a virtual image, as the dotted lines show in Fig. 5b. The magnification of this virtual image can be estimated from simulation using two dipole sources, and the simulated magnification is about  $1.65\times$ , close to the experimental one. Therefore, we propose that the clear and sharper images formed in Figs. 2 and 4 are from the high- $k$  Fourier components. Previous studies on nanoscale and microscale lens imaging have observed the image formed from the large- $k$  Fourier components, the magnification of the image is also about  $1.5\times$  in a

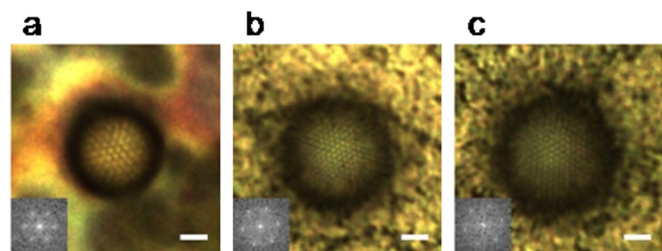


**Figure 4** | Optical images of a semi-immersed microscale lens on a small object at different distance  $d$ . (a)  $d = 0$ . (b)  $d = 3.1 \mu\text{m}$ . (c)  $d = 4.1 \mu\text{m}$ . A virtual image is formed at each of the three distances studied here. The small object is fabricated from the 280 nm PS microspheres. The lens is semi-immersed in the SU-8 resist. The scale bar is  $2 \mu\text{m}$ .



**Table 1** | Comparisons of the magnification  $M$  of both the blurring and clear images among the experimental data, the calculated data by using the  $F$  obtained by ZEMAX, and the calculated data by using the  $F$  obtained by CST. While calculating the magnifications, we first get  $F$  from both ZEMAX and CST. Then, we calculate the magnifications of the images by using the paraxial ray-tracing formulae

$d$ ( $\mu\text{m}$ )	Experimental $M$ of the images (immersed)		Experimental $M$ of the images (not immersed)		Calculated $M$ by using the $F$ obtained from ZEMAX		Calculated $M$ by using the $F$ obtained from CST	
	blurred images	clear images	blurred images	clear images	immersed $F = 5.9$ ( $\mu\text{m}$ )	non-immersed $F = 4.6$ ( $\mu\text{m}$ )	immersed $F = 3.5$ ( $\mu\text{m}$ )	non immersed $F = 3.0$ ( $\mu\text{m}$ )
0	$3.07\times$	$2.08\times$	$4.05\times$	N/A	$1.70\times$	$2.11\times$	$3.31\times$	$5.40\times$
3.1	$-1.64\times$	$1.52\times$	$-1.14\times$	N/A	$15.68\times$	$-5.08\times$	$-1.71\times$	$-1.18\times$
4.1	$-1.19$	$1.51\times$	$-0.85\times$	N/A	$-9.49\times$	$-2.42\times$	$-1.15\times$	$-0.85\times$

semi-immersed case<sup>16</sup>, and near-field magnification plays an important role in the image formation<sup>7,9</sup>. In conclusion, we have demonstrated that when a microscale spherical lens is semi-immersed in a medium, it can intercept more large- $k$  Fourier components. However, the microscale lens images differently for the two Fourier components, and two images corresponding to the two components can be formed simultaneously by the microscale lens.

## Methods

Two-dimensional (2D) polystyrene (PS) microsphere arrays were fabricated by confined convective self-assembly. Centimeter sized uniform and transparent 2D microsphere arrays are formed on the substrate. Then, a 50-nm-thick silver layer was evaporated on the surface of the 2D PS microsphere array by thermal evaporation at a rate of  $1.5 \text{ \AA s}^{-1}$ . For some samples, a SU-8 2000 resist layer of thickness  $d$  was first spin

coated on top of the 2D microsphere array. The SU-8 resist was then exposed, developed, and cross-linked. The thickness of the SU-8 layer could be controlled by using different types of SU-8 resist and different spin speeds. Then, a drop of the diluted 4.87- $\mu\text{m}$ -diameter silica sphere suspension (Bangs Laboratories) was dropped on surface of the silver coated or both silver and SU-8 coated samples. Finally, for some samples, a diluted SU-8 2002 resist (diluted by 50% by using  $\gamma$ -butyrolactone) was spin coated onto the sample at a speed of 3000 rpm for 40 seconds to make the lenses semi-immersed in SU-8. The thickness of the SU-8 layer was measured by a step profiler (ABMios Technology, XP-1). A Leica DM 2500M microscope was used to focus through the silica sphere (microscale lens) into the object, and the formed images were collected by a CCD camera. The light source in the microscope is a white-light source, a halogen lamp. The surface structure of the 2D PS microsphere arrays was characterized by a scanning electron microscope (SEM, Hitachi S-4800). Finite-difference time-domain (FDTD) simulations were carried out using CST program. CST is a commercial FDTD program by calculating the exact solution of Maxwell's equation. The geometrical optical ray tracing analysis was performed using ZEMAX program. In ZEMAX, paraxial ray-tracing formulae are used for computing.

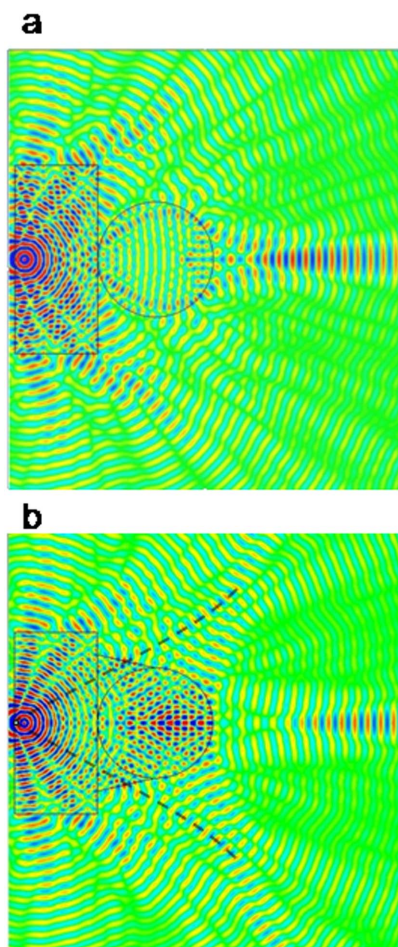


**Figure 5** | CST simulation results of the electric field distribution of a dipole imaged by the microscale lens. (a) The lens is not semi-immersed in the SU-8 resist. (b) The lens is semi-immersed in the SU-8 resist.  $\lambda = 555 \text{ nm}$ .

- Mansfield, S. M. & Kino, G. S. Solid immersion microscope. *Appl. Phys. Lett.* **57**, 2615–2616 (1990).
- Kino, G. S. The solid immersion lens. *SPIE conference on optical engineering for sensing and nanotechnology* **3740**, 2–5 (1999).
- Spillane, S. M., Kippenberg, T. J. & Vahala, K. J. Ultralow-threshold Raman laser using a spherical dielectric microcavity. *Nature* **415**, 621–623 (2002).
- Kapitonov, A. M. & Astratov, V. N. Observation of nanojet-induced modes with small propagation losses in chains of coupled spherical cavities. *Opt. Lett.* **32**, 409–411 (2007).
- Wenger, J., Gerard, D., Aouani, H. & Rigneault, H. Disposable microscope objective lenses for fluorescence correlation spectroscopy using latex microspheres. *Anal. Chem.* **80**, 6800–6804 (2008).
- Schwartz, J., Stavrakis, S. & Quake, S. R. Colloidal lenses allow high-temperature single-molecule imaging and improve fluorophore photostability. *Nat. Nanotechnology* **5**, 127–132 (2010).
- Lee, J. Y. *et al.* Near-field focusing and magnification through self-assembled nanoscale spherical lenses. *Nature* **460**, 498–501 (2009).
- Devilez, A. *et al.* Three-dimensional subwavelength confinement of light with dielectric microspheres. *Opt. Express* **17**, 2089–2094 (2009).
- Wang, Z. *et al.* Optical virtual imaging at 50 nm lateral resolution with a white-light nanoscope. *Nat. Commun.* **2**, 1–6 (2011).
- Yang, S., Taflove, A. & Backman, V. Experimental confirmation at visible light wavelengths of the backscattering enhancement phenomenon of the photonic nanojet. *Opt. Express* **19**, 7084–7093 (2011).
- Darafsheh, A., Walsh, G. F., Negro, L. D. & Astratov, V. N. Optical super-resolution by high-index liquid-immersed microspheres. *Appl. Phys. Lett.* **101**, 141128 (2012).
- Vlad, A., Huynen, I. & Sorin, S. Wavelength-scale lens microscopy via thermal reshaping of colloidal particles. *Nanotechnology* **23**, 285708 (2012).
- Guo, H. *et al.* Near-field focusing of the dielectric microsphere with wavelength scale radius. *Opt. Express* **21**, 2434–2443 (2013).
- Fletcher, D. A. Near-field infrared imaging with a microfabricated solid immersion lens. *Appl. Phys. Lett.* **77**, 2109 (2000).
- Mason, D. R., Jouravlev, M. V. & Kim, K. S. Enhanced resolution beyond the Abbe diffraction limit with wavelength-scale solid immersion lenses. *Opt. Lett.* **35**, 2007–2009 (2010).
- Hao, X., Kuang, C., Liu, X., Zhang, H. & Li, Y. Microsphere based microscope with optical super-resolution capability. *Appl. Phys. Lett.* **99**, 203102 (2011).
- Sasaki, M., Kurosawa, T. & Hane, K. Micro-objective manipulated with optical tweezers. *Appl. Phys. Lett.* **70**, 785–787 (1997).
- Wu, M. H. & Whitesides, G. M. Fabrication of arrays of two-dimensional micropatterns using microspheres as lenses for projection photolithography. *Appl. Phys. Lett.* **78**, 2273–2275 (2001).
- Ye, R. *et al.* Experimental far-field imaging properties of a  $\sim 5\text{-}\mu\text{m}$  diameter spherical lens. *Opt. Lett.* **38**, 1829–1831 (2013).



20. Duan, Y., Barbastathis, G. & Zhang, B. Classical imaging theory of a microlens with super-resolution. *Opt. Lett.* **38**, 2988–2990 (2013).
21. Goldstein, D. J. A quantitative computer simulation of microscopic imaging. *Journal of Microscopy* **162**, 241–253 (1991).
22. Pendry, J. B. Negative refraction makes a perfect lens. *Phys. Rev. Lett.* **85**, 3966–3969 (2000).

## Acknowledgments

This research was partially supported by National Basic Research Program of China (973 Program, 2012CB921801), Doctoral Fund of Ministry of Education of China (Grant No. 20133207110007), and National Natural Science Foundation of China (Grant No. 61205162).

## Author contributions

R.Y. conducted experiments. H.F.M., L.C., J.M., F.W. and R.S. conducted electromagnetic simulations. R.Y., Y.Y. and J.Z. analyzed the data. Y.Y. and J.Z. wrote the manuscript. All authors reviewed the manuscript.

## Additional information

**Supplementary information** accompanies this paper at <http://www.nature.com/scientificreports>

**Competing financial interests:** The authors declare no competing financial interests.

**How to cite this article:** Ye, R. *et al.* Experimental imaging properties of immersion microscale spherical lenses. *Sci. Rep.* **4**, 3769; DOI:10.1038/srep03769 (2014).



This work is licensed under a Creative Commons Attribution-NonCommercial-NoDerivs 3.0 Unported license. To view a copy of this license, visit <http://creativecommons.org/licenses/by-nc-nd/3.0>